remote sensing

MDPI

Article

Insights into Intense Lightning Activity During the Lifetime of Super Typhoon Doksuri (2023)

Xu He [1], Shaohua Gong [1,2,*], Gaopeng Lu [3], Xuewu Cheng [4], Guotao Yang [2], Hailiang Huang [3], Faquan Li [4], Jing Jiao [2] and Zhenquan Yin [1]

[1] School of Physics and Electronics Engineering, Hainan Normal University, Haikou 571158, China
[2] State Key Laboratory of Solar Activity and Space Weather, Beijing 100190, China
[3] School of Earth and Space Sciences, University of Science and Technology of China, Hefei 230026, China
[4] Innovation Academy for Precision Measurement Science and Technology, Chinese Academy of Sciences, Wuhan 430071, China
* Correspondence: shhgong@hainnu.edu.cn

Highlights

What are the main findings?

- Lightning activity in Typhoon Doksuri (2023) exhibited intermittent outbreaks behavior and intense lightning flashes, which were mainly concentrated in the outer rainband of the typhoon.
- Deep convections inside the typhoon provided favorable thermodynamic conditions (i.e., a high CAPE index, abundant water vapor, and a low cloud-top brightness temperature) for the formation of intense lightning via the non-inductive charging mechanism.
- Intense inner-core lightning preceded the typhoon's first intensity peak by 14–41 h; during the re-intensification stage, it occurred ~9 h after the typhoon peak.

What are the implications of the main findings?

- The characteristics and formation mechanisms of the lightning activity during Typhoon Doksuri (2023) were revealed using experimental observations and numerical simulations, improving our understanding of typhoon-associated lightning activity.
- The correspondence between intense lightning phenomena and rapid intensification of the typhoon was investigated, which could contribute to typhoon forecasting and disaster warning in the Western Pacific.

Abstract

The characteristics and formation mechanisms of lightning activity during the lifetime of Super Typhoon Doksuri (2023) were investigated using ERA5 reanalysis data and observation data from the World-Wide Lightning Location Network (WWLLN) and Himawari-8/9 satellite. The lightning activity exhibited pronounced intermittent outbreak behavior, and intense lightning flashes mainly occurred in the outer rainband region approximately 200–600 km from the typhoon center. The occurrence of intense lightning was mainly related to the development of deep convections which were characterized by a high CAPE index and low cloud-top brightness temperature. In the landfall stage, intense lightning outbreaks may have been further modulated by the orographic lifting from the underlying surface and island thermal effects. Strong updrafts within the typhoon provided favorable conditions for intracloud microphysical electrification processes. The formation of intense lightning was interpreted via the non-inductive charging mechanism and

Academic Editor: Carmine Serio

Received: 3 September 2026
Revised: 23 October 2026
Accepted: 30 October 2026
Published: 5 November 2026

Copyright: © 2026 by the authors. Licensee MDPI, Basel, Switzerland. This article is an open access article distributed under the terms and conditions of the Creative Commons Attribution (CC BY) license.

validated using E-WRF model simulations. During the first rapid-intensification episode, intense inner-core lightning preceded the typhoon intensity peak by 14–41 h; during the re-intensification episode, it occurred ~9 h after the typhoon peak. These insights into the intense lightning activity in Super Typhoon Doksuri (2023) contribute to improving typhoon forecasting and disaster warning in the Western Pacific.

Keywords: Typhoon Doksuri; lightning activity; deep convection; non-inductive charging mechanism

1. Introduction

Lightning is a transient atmospheric electrical discharge process that primarily occurs within deep convective clouds, which involves rapid charge transfer, strong currents, and intense electromagnetic radiation [1]. According to the discharge location, lightning flashes can be classified into intracloud lightning and cloud-to-ground lightning. Typhoons are tropical weather systems that contain a large amount of unstable energy. Frequent collisions between hydrometeors (i.e., ice crystals and graupel) may occur within deep convections because of the strong updrafts and downdrafts, and strong electric fields can be formed during particle collisions and separation processes within typhoon cloud systems. The accompanying lightning activity is essentially gas discharge, which is triggered when the local electric field intensity is greater than the breakdown threshold of air. Lightning activity in the typhoon is therefore an important manifestation of deep convective development, and its occurrence is closely related to the complicated dynamic and thermodynamic processes inside typhoons.

Since the pioneering work of Black and Hallett [2], numerous experimental observations and numerical simulations have been conducted on the lightning activity in tropical cyclones (TCs) to characterize their spatiotemporal distribution and possible formation mechanisms [3,4]. Using the observations of the World-Wide Lightning Location Network (WWLLN), Price et al. [5] investigated the statistical characteristics of lightning activity in 56 hurricanes from around the world and found that lightning frequency may be related to intensity changes in typhoons and that strong vertical motion inside typhoons plays a key role in establishing strong electric fields. Similar results were reported by Corbosiero and Molinari [6], Wang et al. [7], and Zhang et al. [8], indicating that lightning activity is associated with changes in the thermodynamic conditions inside typhoons. Moreover, Naccarato et al. [9] and Kumar and Kamra [10] reported that cloud-to-ground lightning density tends to increase during the typhoon landfall process and that lightning activity in TCs presents different characteristics compared to cloud-to-ground lightning due to the different underlying surfaces and to island thermal effects. Regarding lightning activity in the typhoon inner-core region, research from Abarca et al. [3] and Zhang et al. [11] found that intense lightning outbreaks typically occurred ahead of the typhoon intensity peak, approximately 24–48 h before, thus serving as an indicator of rapid intensification of the typhoon. To study the microphysical processes of lightning in thunderstorms, Fierro et al. [4] developed the E-WRF (Weather Research and Forecasting model with electrification) model by coupling the explicit electrification and lightning parameterization schemes within the WRF system and successfully simulated the intracloud charge structure and lightning activity within convective clouds. Subsequently, Lu et al. [12] applied this model to accurately simulate lightning processes in typhoons, including the microphysical processes of charge transfer and distribution in convective clouds. Their results confirmed that the charge separation originates from the collisions between ice crystals and graupel under suitable conditions. Recently, based on the diffusion of protons (H^+) in

ice crystals and the L-defect trapping mechanism, Kang et al. [13] proposed a new charge-separation model, trying to further characterize the microphysical electrification processes inside typhoon cloud systems.

Although considerable progress has been made in recent decades, the current understanding of the characteristics of lightning activity in TCs is still not comprehensive enough, and evidence for the proposed microphysical mechanisms is also lacking. Due to limitations of current observation methods, direct observational data on typhoon activity and the internal lightning phenomena are relatively scarce, and the theories on these processes have not been adequately verified experimentally. In addition, since typhoons are constantly moving and changing over time, lightning phenomena occur at different stages of typhoon development and may thus be driven by different formation mechanisms and exhibit unique characteristics. To analyze lightning activity in different typhoons, more experimental observations and further model simulations are needed. Super Typhoon Doksuri (2023) is one of the strongest typhoons to have made landfall on the Chinese mainland in recent years, and the accompanying lightning activity exhibited varying characteristics at the rapid intensification, landfall, and remnant-vortex northward-maintenance stages. In this study, using ERA5 reanalysis data and observations from the WWLLN and Himawari-8/9 satellite, the characteristics of the lightning activity during Typhoon Doksuri (2023) were investigated, and the possible formation mechanisms for the intense lightning outbreaks at the various stages are discussed. Although it is a case study, the results contribute to our understanding of lightning phenomena in Western Pacific typhoons and to typhoon monitoring and disaster warning in coastal areas.

2. Materials and Methods

According to the TC best-track dataset from the China Meteorological Administration (CMA, http://www.nmc.cn, accessed on 2 September 2026), Doksuri (2023) formed in the Western Pacific and intensified into a typhoon over the ocean near the Philippines on 23 July 2023. It became a super typhoon around 20 UT on 24 July, with a maximum wind speed of ~58 m/s. On 26 July, it made landfall over the Babuyan Islands and subsequently weakened into a severe typhoon. On 27 July, Typhoon Doksuri re-intensified into a super typhoon while it traveled over the South China Sea. Typhoon Doksuri made landfall at Jinjiang City on 28 July and then gradually weakened as it moved inland. The typhoon track is plotted with line segments in Figure 1, and its intensity variation is shown by the color gradient. The typhoon center locations at 00 UT are shown and marked with the date. The resolution of the position and intensity information of this track dataset over the Northwest Pacific is 6 h, and it starts 3 h after landfall [14].

The WWLLN is a positioning system that uses globally distributed very-low-frequency (VLF, 3–30 kHz) electromagnetic monitoring stations to detect the electromagnetic pulse signals radiated by lightning. Cloud-to-ground lightning with a high radiation intensity can be detected under all weather conditions, with errors of typically less than 10 km in the recorded position data and a temporal precision of about 10 μs [15,16]. The WWLLN observations can be used to study the lightning activity during the whole lifetime of Typhoon Doksuri (2023). Lightning flashes within 1000 km of the typhoon center were analyzed, and the lightning density (flashes per 100 km^2) for each geographical location was calculated and marked on the map. In the WWLLN's lightning strike raw data, a complete lightning flash usually contains multiple strokes. Therefore, during the data analysis, the raw data were first clustered according to the time interval and spatial distance between the discharge events using a sequential clustering algorithm similar to that of Zhang et al. [17] and Zhu et al. [18]. For any two different strokes, if the time interval is ≤0.5 s and the spatial distance is ≤10 km, they were classified as the same lightning flash. Meanwhile, the time-span threshold between the first and last strokes within the same

flash was set to less than 1 s. The stroke with the greatest far-field energy was used to represent the whole cluster, and the lightning flash was characterized with the spatiotemporal information (i.e., longitude, latitude, and occurrence time) of the strongest stroke. On the other hand, since the lightning flash is positioned according to the "time difference in arrival" in the WWLLN records, only lightning flashes detected simultaneously by more than five stations (nstn ≥ 5) were analyzed, ensuring that the lightning locations were precisely detected. In recent years, with the increase in the number of sensors and the upgrading of the positioning algorithm, the detection performance of the WWLLN has continuously improved, and the positioning accuracy and detection efficiency can be typically reach about 5 km and 11%, respectively [19,20]. Here, for the detection of lightning flashes during Typhoon Doksuri (2023), these preset spatial and temporal criteria are reasonable, and they allowed us to effectively avoid double counting. In addition, to calculate the lightning density, typhoon track data were interpolated with a temporal resolution of 1 h via the cubic-spline interpolation method, and the lightning occurring within 30 min before and after each time point was counted as the number of flashes within that time interval. The spatial distribution of lightning flashes was gridded at a resolution of 0.2° × 0.2°, and the lightning density was calculated for each grid cell.

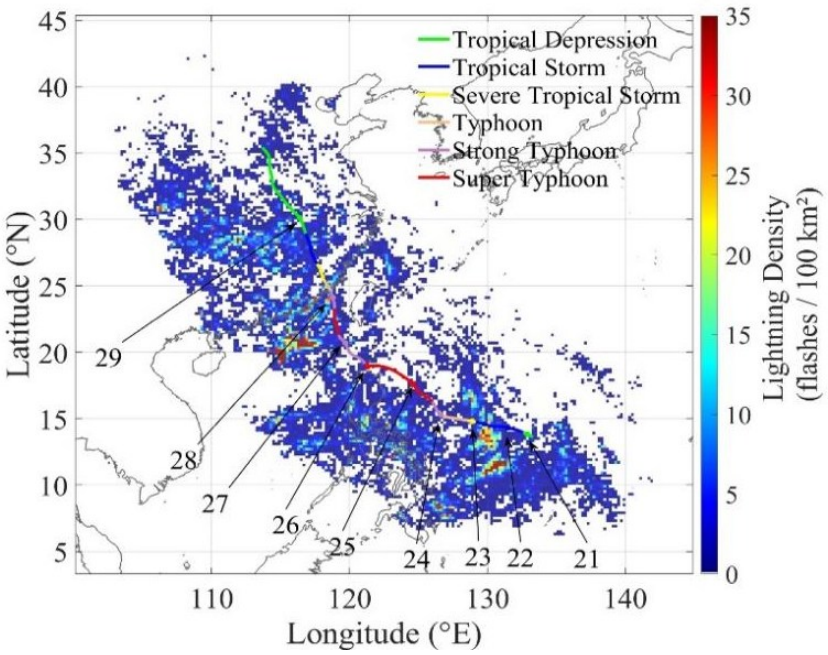


Figure 1. Distribution of the accumulated lightning flash density within 1000 km of Typhoon Doksuri's center during 21–30 July 2023. The typhoon track is plotted with solid line segments, and its intensity variations are illustrated by the color gradient. Typhoon center locations at 00 UT of each day are marked with the date.

ERA5 reanalysis data were taken from the European Centre for Medium-Range Weather Forecasts (ECMWF), and atmospheric thermodynamic parameters (e.g., temperature and humidity) were used to analyze typhoon activities [21]. Here, convective available potential energy (CAPE), pseudo-equivalent potential temperature (θ_e), and cloud-top brightness temperature were employed to verify the correlation between the lightning activity and thermodynamic processes within the typhoon. The horizontal spatial resolution was 0.25° × 0.25°, and the temporal resolution was 1 h.

Himawari is a geostationary satellite launched by the Japan Meteorological Agency (JMA). Its advanced Himawari imager (AHI) has a total of 16 observation channels (3 visible channels, 3 near-infrared channels, and 10 infrared channels), with center

wavelengths covering the 0.47–13.3 μm band, that covers the area of 80°E–160°W, 60°N–60°S [22]. Typhoon activities in the Western Pacific can be effectively monitored via continuous observation with high spatiotemporal resolutions [23,24]. Here, the observation data from Channel 16 (13.3 μm) were used to analyze the variations in cloud-top brightness temperature (temperature of black body, TBB) of the convective structures. To identify the changes in the cloud phase state, the brightness-temperature difference (BTD [11–14]) between the measurements from Channel 11 (8.6 μm) and Channel 14 (11.2 μm) was calculated to detect the ice-phase particles at the top of clouds [22,25]. These observation data typically have a spatial resolution of 2 km and a temporal resolution of 10 min.

For the lightning activity analysis at different stages, because the scale and intensity of the strong convective boundary of Typhoon Doksuri continuously changed over time [17], this boundary had to be dynamically extracted using the data analysis method of Zhu et al. [18] and the cloud-top brightness temperature (TBB) data from Himawari-8/9 and the tropical cyclone best-track dataset from CMA. For example, the strong convective boundary of Typhoon Doksuri around 00 UT on 27 July 2023 was extracted as shown in Figure 2, and the lightning flashes occurring within the strong convective boundary are correspondingly marked on the cloud image.

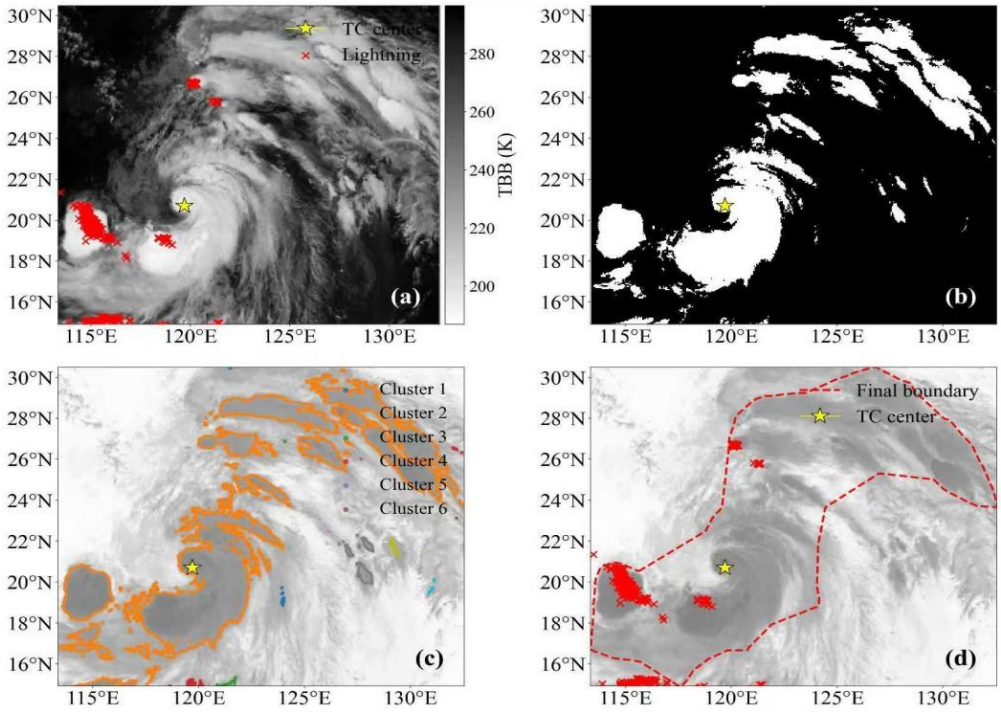


Figure 2. Extraction process of the strong convective boundary of Typhoon Doksuri around 00 UT on 27 July 2023. (**a**) Himawari-8/9 satellite cloud image with the typhoon center (yellow star) and lightning flashes (red crosses), (**b**) binarized TBB image, (**c**) clustering results of the convective clouds (six clusters are marked with different colors), and (**d**) the fitted strong convective boundary (i.e., the red dashed line).

In this study, the TBB data covering the typhoon cloud system were first selected, and lightning flashes occurring within the 30 min before and after the time point of interest were marked at their corresponding positions on the cloud image (i.e., Figure 2a). To highlight the pixels in the region where the strong convective system was located, the TBB cloud image was binarized using 228 K as a threshold (Figure 2b), following the same criterion adopted by Zhu et al. [18]. This threshold is comparable to the typical TBB values of deep convective clouds embedded in typhoon cloud systems, and the strong convective areas can be effectively separated from the surrounding stratiform and cirrus regions. The

Roberts operator was used to identify edge pixels in the binarized TBB image, and the detected edge points were clustered via the DBSCAN method [26]. Figure 2c shows the TBB distribution at this moment, which was classified into 6 different clusters, each marked with a different color. The centroid was calculated for each cluster, and the distance between the centroid and the typhoon center was estimated, with only those clusters with a distance less than 1000 km retained for the subsequent analysis. After the convective cloud systems were clustered, convex-hull and concave-hull fittings (i.e., Alpha Shape fitting) were performed on the boundary points (Figure 2d), and all lightning flashes were marked at the corresponding positions on the cloud image. Considering the probable errors introduced during the data analysis, the obtained boundary of the strong convection region was expanded outward by 10 km, which is comparable to the pixel size of the edge detection process and to the typical WWLLN location error (~10 km) [15,16]. Finally, the strong convective boundary within the typhoon around 00 UT on the 27th was obtained and is indicated by dashed lines in Figure 2d.

To simulate the intracloud electrical processes and lightning activity, the electrification module developed by Fierro et al. [4] was implemented into the WRF model. In this study, the WRF_4.3.1 model was employed; the configuration schemes for the main physical parameterization are listed in Table 1, and the domain boundaries are shown in Figure 3. The NSSL microphysics scheme was employed to simulate intracloud electrical processes and lightning activity, and the variations in mixing ratios (or number concentrations) of cloud droplets, raindrops, ice crystals, snow, graupel, and hail (i.e., six categories of hydrometeors) were investigated. Inductive and non-inductive charging modules were enabled in the innermost grid region, and the charge density and electric field distribution in the typhoon cloud systems were simulated within the deep convection process [27]. A three-layer nested grid was used during the numerical simulation process, with the horizontal resolutions are set to 6, 2, and 1 km, respectively. In the vertical direction, 47 layers were selected, and the maximum altitude was set at ~50 hPa. Based on the analysis results from Sakradzija et al. [28] and Bian et al. [29], the cumulus convection parameterization scheme was turned off during the numerical simulation in this study, since the selected inner nested grid regions are presented with extremely high resolutions (2 km and 1 km). In addition, the model simulations were initialized at 18 UT on 26 July 2023 and integrated until 02 UT on 27 July 2023. Here, a 6 km horizontal resolution was not considered the gray zone, and deep convections on the outer domain (d01) could be poorly resolved without cumulus convection parameterization. For this reason, a sensitivity experiment was carried out and the comparison results showed that when the cumulus scheme was turned off, the model-simulated typhoon path was close to the reported CMA best track, and the large-scale moisture and momentum supply to the inner domains were not materially affected by this treatment.

Table 1. Physical parameterization schemes and model configurations used in the E-WRF simulation of Typhoon Doksuri.

Parameter	Settings
Horizontal resolution	6 km, 2 km, 1 km
Vertical levels	47
Model top	50 hPa
Time step	30 s (d01), 10 s (d02), 5 s (d03)
Grid points	105 × 87 (d01), 283 × 229 (d02), 545 × 437 (d03)
Boundary-layer scheme	YSU [30]
Longwave radiation scheme	RRTMG [31]
Shortwave radiation scheme	Dudhia [32]
Microphysics scheme	NSSL [33]

Cumulus convection parameterization scheme	None [28,34]
Land surface scheme	Noah [35]
Surface-layer scheme	MM5 [36]

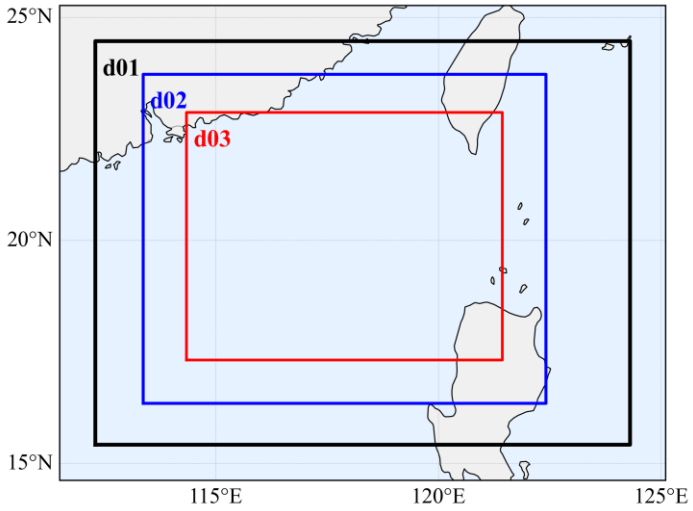


Figure 3. Nested domains of the E-WRF simulation for Typhoon Doksuri. The black, blue, and red boxes denote the domains of d01, d02, and d03, and their horizontal resolutions are 6 km, 2 km, and 1 km, respectively.

3. Results and Discussion

3.1. Statistical Characteristics of Lightning Activity

The statistical results for the lightning-density distribution during Typhoon Doksuri are plotted in Figure 4. The lightning activity exhibited pronounced intermittent outbreak behavior, and intense lightning mainly occurred in the outer rainband region approximately 200–600 km from the typhoon center. The intense lightning occurred in two time periods: from 10 UT on the 23rd to 18 UT on the 25th and from 16 UT on the 26th to 04 UT on the 28th. Similar intermittent outbreak behavior of lightning activity in TCs was reported by Squires and Businger [37], and they suggested that the occurrence of intense lightning is closely related to the rapid intensification of the typhoon. The time-dependent minimum central pressure (MCP) of Typhoon Doksuri is plotted in Figure 4, which shows that the MCP of typhoon decreased rapidly between the 23rd and 25th, and the intense lightning occurred in the outer rainband (i.e., about 200–600 km from the typhoon center) in the same time period, indicating that the occurrence of intense lightning occurred simultaneously with the rapid intensification of the typhoon. In the second period (16 UT on the 26th to 04 UT on the 28th), Typhoon Doksuri experienced a reinforcement process over the South China Sea before entering the final landfall stage. In the rapid reinforcement stage (00–14 UT on the 27th), there was a good correspondence relationship between intense lightning occurrence and the rapid intensification of the typhoon. However, the intense lightning outbreaks that occurred after 14 UT on the 27th occurred during the landfall stage of Doksuri, which corresponded to a rapid decrease in the typhoon's intensity. Thus, the occurrence of intense lightning was indeed closely related to the rapid intensity changes in Typhoon Doksuri, with intense lightning outbreaks occurring not only during the rapid intensification process but also in the landfall stage.

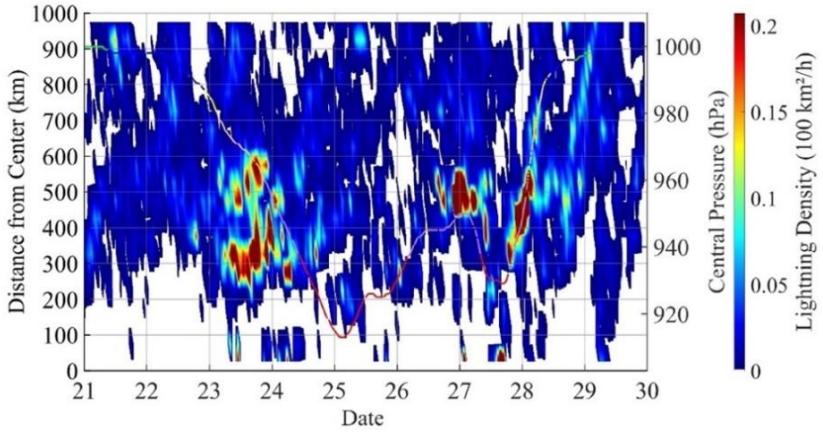


Figure 4. Statistical results of the lightning-density distribution during Typhoon Doksuri activity. The number of hourly lightning flashes occurred in each 100 km² is plotted with different colors. The curve shows the time-dependent minimum central pressure (MCP) of the typhoon, and the intensity variation in the typhoon is illustrated by the color gradient (the same as Figure 1).

3.2. Intense Lightning Occurred in the Outer Rainband

The occurrence of lightning flashes in typhoons indicates the establishment of a strong intracloud electric field and the subsequent air-breakdown processes, which are often related to the complicated thermodynamic processes in typhoon systems [38,39]. For example, in this study, the strongest lightning event occurred in the outer rainband around 00 UT on 27 July according to ERA5 reanalysis data and satellite observations. The spatial distribution of atmospheric parameters—convective available potential energy (CAPE), equivalent potential temperature θ_e at 850 hPa, and cloud-top brightness temperature—was also verified for the lightning flashes shown in Figure 5. Around 00 UT on 27 July, the center of Typhoon Doksuri was located at 21°N, 120°E, and it was in the early stage of re-intensification (Figure 1), with intense lightning flashes (marked as white crosses) occurring at 18–21°N, 114–117°E. The strong convective boundary was extracted (Figure 2) and is marked as a white dashed line in Figure 5. Figure 5a shows that intense lightning occurred within the typhoon's strong convective boundary, and the atmospheric CAPE index around this intense lightning region was in the range of 3500–5000 J/kg, meaning that the atmosphere was in an extremely unstable state. Figure 5b shows the spatial distribution of equivalent potential temperature θ_e at the 850 hPa isobaric surface. In the region with intense lightning, θ_e > 350 K, indicating that the lower atmosphere in this region was characterized by a high temperature and high humidity [40]. The satellite TBB image in Figure 5c shows that the cloud-top brightness temperature in the intense lightning region was extremely low at this moment, with a minimum of ~195 K. Altogether, the analysis results indicate that the satellite-observed clouds with extremely low temperatures were convective clouds, and the occurrence of intense lightning outbreaks was closely related to deep convection activities in the outer rainband of the typhoon.

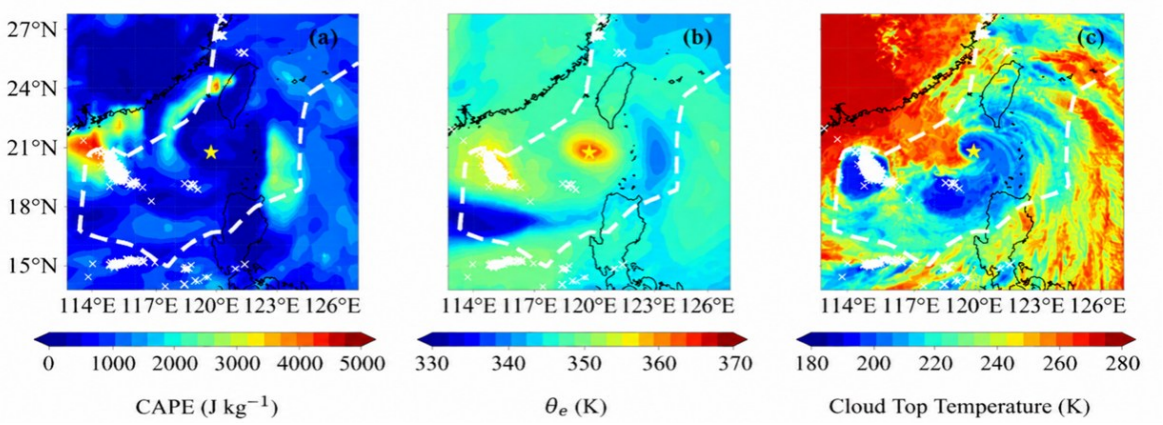


Figure 5. Spatial distribution of atmospheric thermodynamic parameters around 00 UT on 27 July 2023: (**a**) CAPE index (J kg^{-1}), (**b**) pseudo-equivalent potential temperature θ_e at 850 hPa, and (**c**) cloud-top brightness temperature. In all panels, the typhoon center is marked with a yellow star, the strong convective boundary is marked by the dashed white line, and the lightning locations are denoted by white crosses.

During typhoon activity, extreme deep convection may provide favorable thermodynamic conditions for intracloud microphysical electrification processes, and ice crystals and graupel particles with different charges can be generated due to the strong upward motions [41]. Figure 6 shows that extreme deep convections were accurately observed by the Himawari-8/9 satellite around 00 UT on 27 July, and a large number of rapid "upwelling" clouds with extremely low TBBs occurred in the intense lightning regions (Supplementary Materials, Python script 1: BTD.py). In particular, the measurements from the 8.6 and 11.2 μm channels reveal that the minimum brightness temperature was less than 180 K in the region of 18–21°N, 114–117°E, indicating that an "anvil cloud" structure had formed in the tropopause region at this moment due to the deep convection. Moreover, the cloud-top brightness-temperature difference (BTD) between the two channels' measurements was greater than 1.5 K in this region (Figure 6c). In general, the BTD is sensitive to the ice-phase cloud particles, with a TBB (11.2) lower than 235 K and BTD [8.6–11.2] greater than 0.5 K indicating ice-phase clouds [20,23]. Combined with the observation results from the Himawari-8/9 satellite, it can thus be inferred that many ice-crystal particles existed at the top of deep convective clouds, and the occurrence of intense lightning in the outer rainband was closely related to the extreme deep convections.

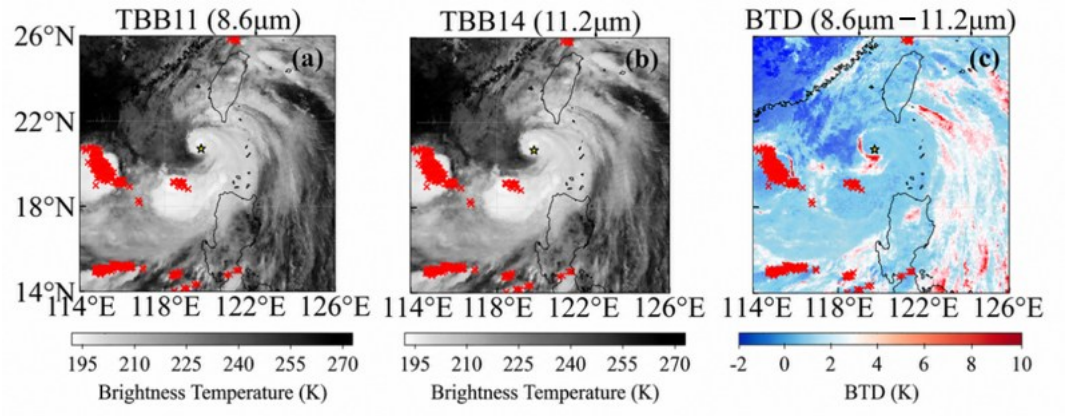


Figure 6. Cloud-top brightness temperature measured by Himawari-8/9 for Typhoon Doksuri activity around 00 UT on 27 July 2023: (**a**) 8.6 μm channel, (**b**) 11.2 μm channel, and (**c**) brightness temperature difference BTD [8.6–11.2] between the two channels. In all panels, the typhoon center is marked with a yellow star, and lightning locations are marked with red crosses.

To further verify the correlations observed between intense lightning outbreaks and extreme deep convections, the spatial distribution of atmospheric microphysical parameters was simulated with the E-WRF model (Supplementary Materials, Python script 2: WRF_ELEC.py) using the physical parameterization schemes listed in Table 1. Figure 7a shows that in the region of 19–21°N, the atmospheric vertical velocity ω was positive at altitudes of 2–15 km, with a maximum of ~6 m/s; that is, the air maintained an updraft in the region with the intense lightning outbreak. It should be noted that this model outputs maximum vertical velocity (~6 m/s) as a cross-section-averaged value, and the instantaneous updrafts in convective cores were considerably stronger. This was independently confirmed by the observation images from Himawari-8/9 for the same time points (Figure 6). The simulation results are consistent with the analysis results shown in Figures 5a and 6. The simulated water vapor distribution (Figure 7b) shows that the maximum water vapor mixing ratio reached ~7.8 g/kg in the temperature layer between 0 and −20 °C (altitude of 5–8 km), indicating that the abundant water vapor provided a sufficient source for the deposition growth and riming process of the ice-phase particles during the satellite-observed upwelling motions. The spatial distribution of ice particles and graupel particles is plotted in Figure 7c,d, respectively. The maximum mixing ratios were 0.54 and 1.0 g/kg, respectively, in the altitude range of 5–15 km, proving that large amounts of ice particles and graupel particles were indeed generated due to the deep convections. Moreover, the intracloud electric field was simulated with the E-WRF model for the region of 18–22°N, 115–120°E, and the spatial distribution of the charge density and electric field is shown in Figure 8. The vertical distribution of total charge density (Figure 8a) presented a typical "positive–negative–positive" tripole charge distribution structure. Negative charges occurred at the temperature layer between 0 and −20 °C (altitude of 5–8 km), and positive charges were distributed above and below this temperature layer. In Figure 8b, the simulated electric field on the 495 hPa surface (altitude of about 5.6 km) shows that a strong electric field existed in the region of 19–20°N, 116–117°E, and the maximum field reached ~150 kV m^{-1}. This is a point maximum within the cross-section rather than a grid-cell mean, and this maximum is comparable to the typical breakdown thresholds (100–150 kV/m) that were actually observed within thunderstorm clouds at similar altitudes [38,39], indicating that the intracloud electric field established via constant charge accumulation was strong enough to trigger intense lightning.

Combining the analysis results shown in Figures 5–8, it can be concluded that the occurrence of the intense lightning on the left side of Figure 5 can be attributed to the deep convective activity in the outer rainband of the typhoon. During the strong upward motion (Figure 6), abundant water vapor provided a sufficient source for the generation of ice-phase particles, and then graupel particles settling due to gravity collided with the ascending ice crystals and completed charge exchange within the low-temperature layer (i.e., between 0 and −40 °C), ultimately forming the typical "positive–negative–positive" tripole charge distribution structure inside the deep convective clouds, and intense lightning was triggered, while the established intracloud electric field was stronger than the breakdown thresholds. This is a typical intense lightning phenomenon that is accompanied by deep convections during typhoon activity, and its outbreak can thus be interpreted using the non-inductive charging mechanism. For the intense lightning flashes near 15°N in Figure 5, they occurred outside the strong convective boundary, and their occurrence should not directly correlate with the atmospheric activities inside the main cloud system of the typhoon.

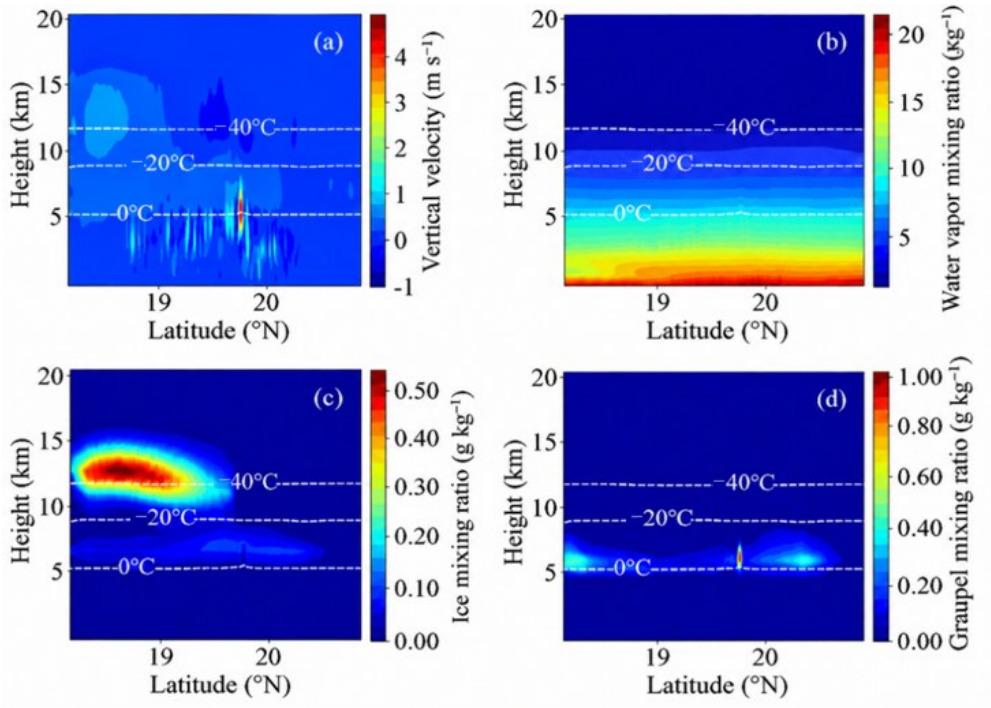


Figure 7. Vertical distribution of microphysical parameters simulated with the E-WRF model: (**a**) atmospheric vertical velocity ω, (**b**) water vapor mixing ratio, (**c**) ice mixing ratio, and (**d**) graupel mixing ratio. The 0 °C, −20 °C, and −40 °C isotherms are marked with dashed lines in all panels.

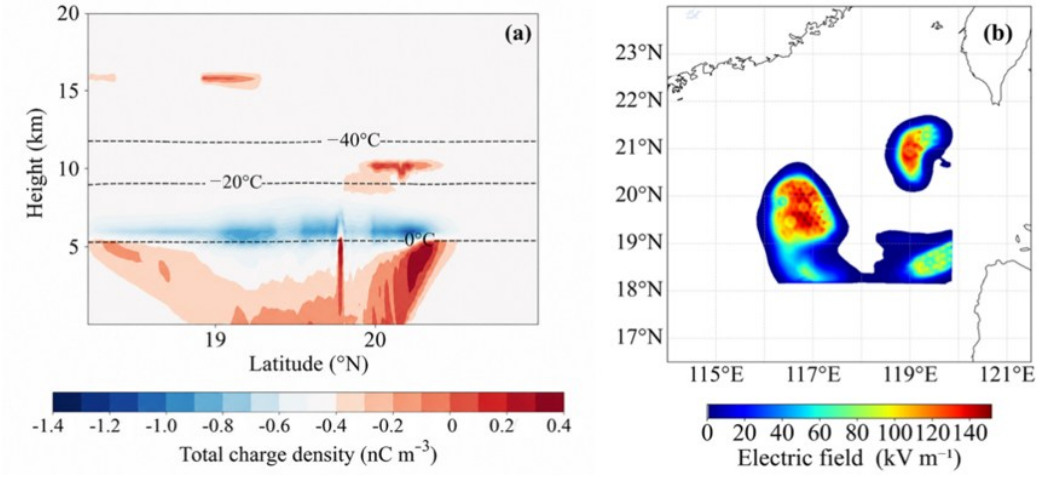


Figure 8. Intracloud electric field simulated by the E-WRF model in the region of 18–22°N, 115–120°E around 00 UT on 27 July 2023. (**a**) Vertical distribution of total charge density and (**b**) horizontal distribution of electric field on the 495 hPa surface. The 0 °C, −20 °C, and −40 °C isotherms are marked with dashed lines in panel (**a**).

Next, the intense lightning phenomena that occurred in the outer rainband (Figure 4) at 18 UT on the 23rd and at 03 UT on the 28th were analyzed. The center of Typhoon Doksuri was located at 15°N, 127°E around 18 UT on the 23rd, and intense lightning occurred simultaneously in the outer rainband (200–600 km) to the southwest and southeast of the typhoon center (Figure 9). At this moment, the typhoon was in the rapid intensification stage (Figure 1), and its outer rainband approached Luzon Island in the southwest direction of the typhoon center. The atmospheric thermodynamic conditions for the intense lightning occurrence in these two regions were determined: around the intense lightning flashes to the southeast of the typhoon center, the maximum CAPE index was greater than 3500 J/kg, the cloud-top brightness temperature was 185–200 K, and the potential

temperature θ_e was higher than 340 K. Moreover, Himawari-8/9 observations show that typhoon clouds in this region were undergoing relatively strong upwelling motions. Similar to the intense lightning phenomenon shown in Figure 5, the occurrence of intense lightning in this region can be attributed to the deep convections in the outer rainband of the typhoon. However, for the intense lightning over Luzon Island, no extreme atmospheric thermodynamic conditions were found (Figure 9), and the CAPE index was less than 1800 J/kg and the cloud-top brightness temperature was higher than 220 K. Thus, the intense lightning flashes above Luzon Island cannot be simply attributed to the extreme thermodynamic instability in the outer rainband, although intense lightning flashes did also occur inside the strong convective boundary. According to the typhoon track information (Figure 1), around this time point, the spiral rainband of Doksuri swept over Luzon Island while the typhoon was moving northwestward. The local underlying-surface forcing may have contributed to these outbreaks, and the near-shore frictional convergence associated with the landfalling rainband may have strengthened the local updrafts [8,10]. That is, the orographic lifting over Luzon Island and the island thermal effect may be plausible additional modulators, but the 0.25° ERA5 data cannot resolve these processes [42,43].

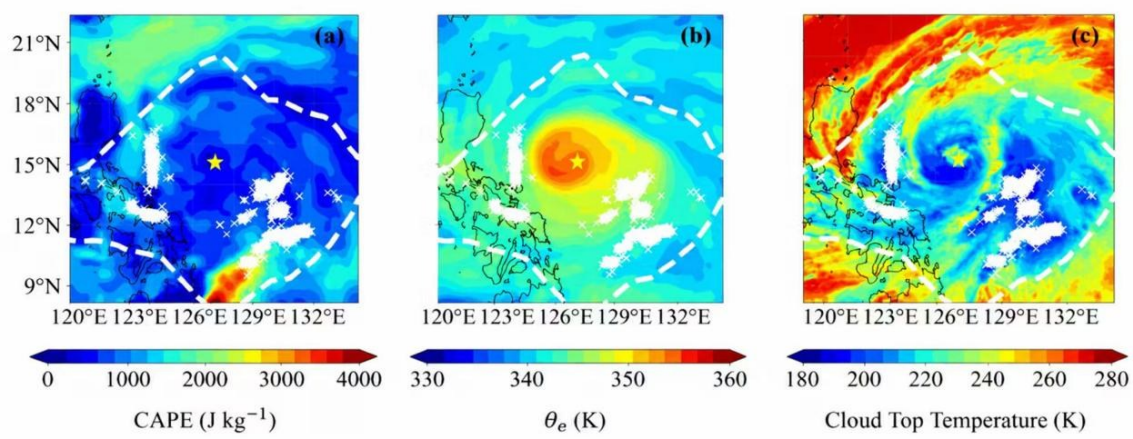


Figure 9. Spatial distribution of atmospheric thermodynamic parameters for the intense lightning phenomenon around 18 UT on 23 July 2023: (**a**) CAPE index (J kg^{-1}), (**b**) pseudo-equivalent potential temperature θ_e at 850 hPa, and (**c**) cloud-top brightness temperature. In all panels, the typhoon center is marked with a yellow star, the strong convective boundary is marked by the dashed white line, and the lightning locations are denoted by white crosses.

The atmospheric thermodynamic conditions around the intense lightning phenomenon that occurred around 03 UT on 28 July and the analysis results are shown in Figure 10. The ambient potential temperature θ_e was maintained at a high temperature of 350–360 K (Figure 10b), the cloud-top brightness temperature was below 210 K (Figure 10c), and the maximum CAPE index was less than 1000 J/kg (Figure 10a). These results indicate that the lower atmosphere was characterized by a high temperature and high humidity, while it maintained a relatively stable thermodynamic state in the vertical direction. Therefore, the occurrence of intense lightning flashes was not directly related to strong deep convection inside the typhoon, although they also occurred inside the strong convective boundary. At this time point, Typhoon Doksuri was in the landfall stage, with its center located at 25°N, 118°E. Similar to the analysis results for the intense lightning that occurred above Luzon Island (Figure 9), local intracloud microphysical processes may have been modified by the effects of underlying-surface forcing and thermal islands, and favorable conditions facilitated the formation of intense lightning [8,43].

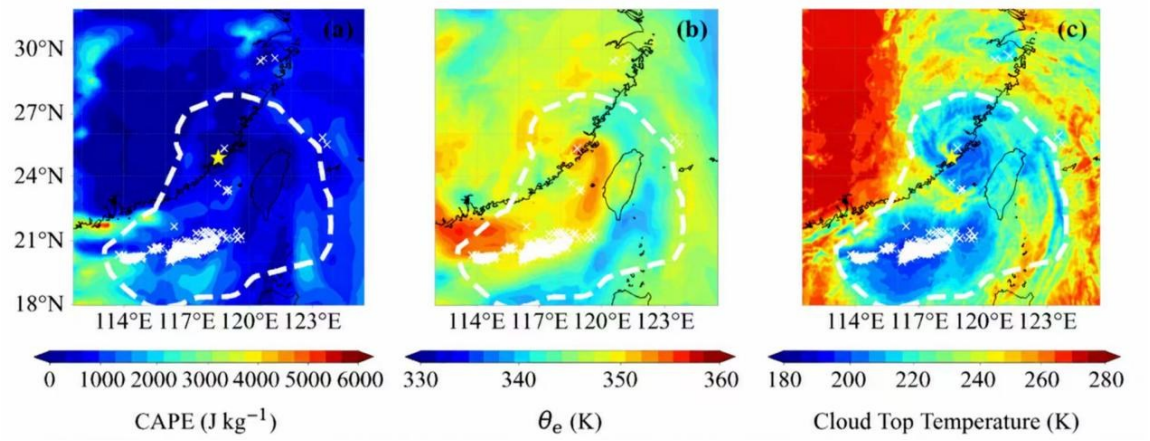


Figure 10. Spatial distribution of atmospheric thermodynamic parameters for the intense lightning phenomenon around 03 UT on 28 July 2023: (**a**) CAPE index (J kg^{-1}), (**b**) pseudo-equivalent potential temperature θ_e at 850 hPa, and (**c**) cloud-top brightness temperature. In all panels, the typhoon center is marked with a yellow star, the strong convective boundary is marked by the dashed white line, and the lightning locations are denoted by white crosses.

3.3. Intense Lightning Occurred in the Inner-Core Region

Some of the observational and theoretical analysis results indicate that during rapid intensification, typhoon development may be accompanied by intense lightning outbreaks in the inner-core region, thus serving as an auxiliary diagnostic signal in typhoon forecasting [11,44]. In this study, the correspondence between the inner-core lightning phenomena (flashes within 100 km of the typhoon center (Figure 4)) and changes in typhoon intensity was investigated; the results are shown in Figure 11. During both rapid intensification processes of Typhoon Doksuri (corresponding to the rapid decreases in the MCP curve), intense lightning phenomena occurred in the inner-core region, namely in the time period from 06 UT on 23 July to 00 UT on 25 July. During this period, Doksuri intensified rapidly from a typhoon into a super typhoon (shown in Figure 1), the MCP rapidly decreased to ~915 hPa (Figure 11), and intense lightning flashes occurred in the inner-core region with a maximum lightning frequency of 38 flashes/hour. During 01–17 UT on 27 July, Typhoon Doksuri re-intensified over the South China Sea, the MCP rapidly decreased from 950 to ~928 hPa, and intense lightning flashes occurred again in the inner-core region.

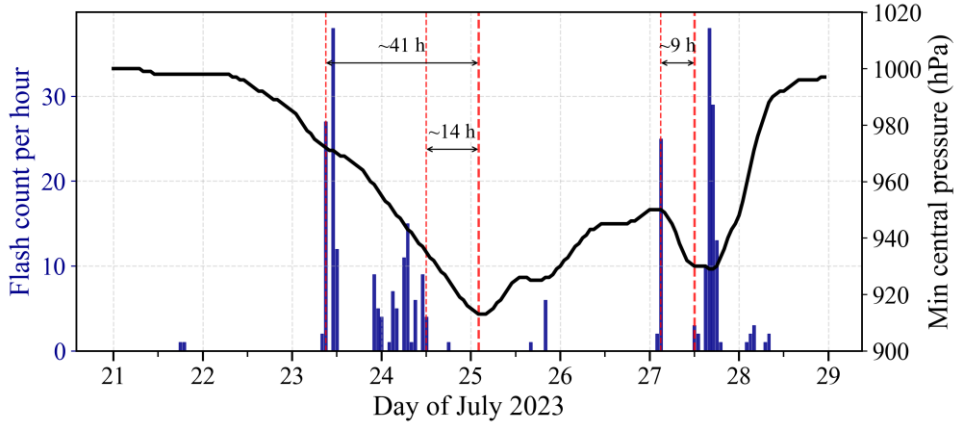


Figure 11. Statistics of hourly lightning flashes (blue bars) in the inner-core region (0–100 km from the center) of Typhoon Doksuri during 21–29 July 2023. The solid black curve shows the time-dependent minimum central pressure (MCP) of the typhoon. Time intervals between the intense lightning flashes and the typhoon intensity peaks are marked with dashed red lines.

Next, the occurrence of the intense lightning outbreaks was investigated by verifying the atmospheric thermodynamic conditions inside the typhoon. Continuous upwelling motions in the inner-core region were observed by the Himawari-8/9 satellite (@8.6 and 11.2 μm channels) around 08:40 UT on 23 July, and the TBB of deep convective clouds was lower than 191 K, and the BTD [8.6–11.2] was greater than 0.5 K (Figure 12). Moreover, intense lightning flashes occurred at the boundary of the deep convective cloud layers. Similar to the analysis results shown in Figure 5, the intense lightning outbreaks that occurred around 08:40 UT on 23 July (Figure 12) were mainly attributed to the drastic upwelling motions in the inner-core region during the typhoon's rapid intensification.

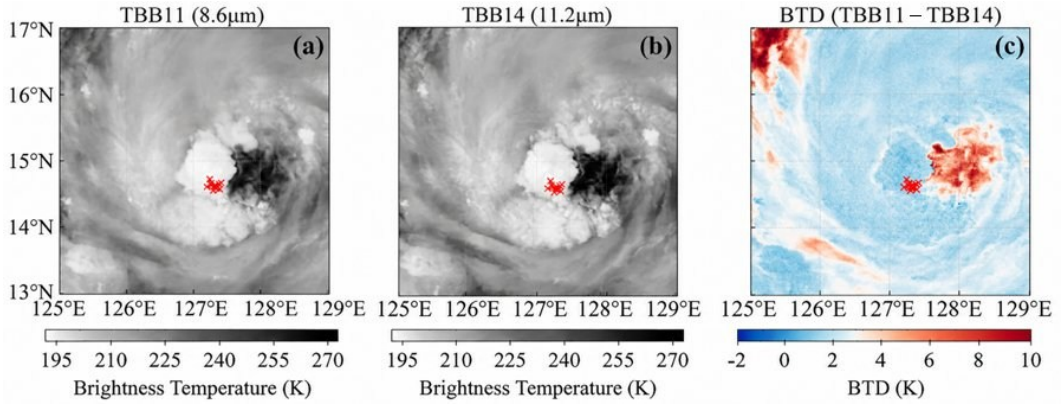


Figure 12. Cloud-top brightness temperature in the inner-core region observed by Himawari-8/9 around 08:40 UT on 23 July 2023: (**a**) 8.6 μm channel, (**b**) 11.2 μm channel, and (**c**) brightness temperature difference BTD [8.6–11.2] between the two channels. In all panels, lightning locations are marked with red crosses.

The intense lightning flashes that occurred in the inner-core region during 01–17 UT on 27 July were analyzed. Typhoon Doksuri experienced a small-scale eyewall replacement during this time period, and the TBB values of spiral updraft clouds outside the eyewall and subsiding airflow inside the eyewall were BT(11.2) ≤195 K and BT(11.2) > 240 K, respectively. This special atmospheric environment formed during the adjustment of the typhoon's internal structure, and the spiral updrafts outside the eyewall may have provided favorable thermodynamic conditions for non-inductive electrification. In fact, Figure 13c shows that these intense lightning flashes occurred in the convergence region of the inner and outer airflows, and the BTD [8.6–11.2] values were 0–0.5 K in this region. Therefore, these intense lightning flashes that occurred in the re-intensification stage (01–17 UT on 27 July) should be related to the pronounced adjustment of the typhoon's internal structure rather than the rapid intensification process.

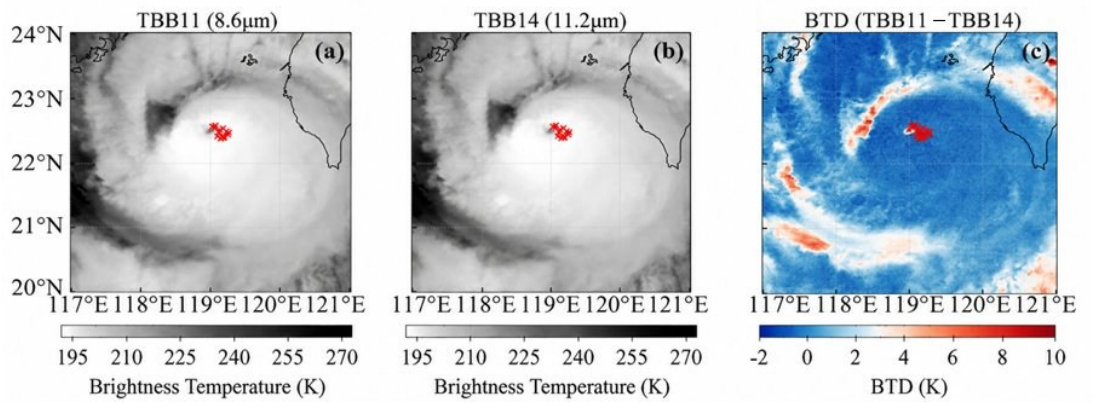


Figure 13. Cloud-top brightness temperature in the inner-core region observed by Himawari-8/9 around 16:10 UT on 27 July 2023: (**a**) 8.6 μm channel, (**b**) 11.2 μm channel, and (**c**) brightness temperature difference BTD [8.6–11.2] between the two channels. In all panels, lightning locations are marked with red crosses.

Indeed, during rapid intensification or eyewall replacement, typhoons are often accompanied by intermittent intense lightning in the inner-core region, and these lightning outbreaks can serve as an auxiliary diagnostic signal [3,11]. Price et al. [5] found that there was a temporal correlation between intense lightning phenomena in the inner-core region and the rapid intensification of the typhoon and that the occurrence of intense lightning was typically detected ahead of the maximum hurricane intensity by ~24 h. A similar conclusion was made by Fierro et al. [45] in their analysis of the rapid intensification of Atlantic Hurricanes Rita and Katrina (2005); they reported that the occurrence of intense lightning in the inner-core region preceded the typhoon intensity peak by 24–48 h. Regarding the inner-core intense lightning outbreaks during Typhoon Doksuri, the maximum hourly flash count preceded the typhoon intensity peak by about 14–41 h during the first rapid-intensification episode, whereas it occurred ~9 h after the typhoon peak during the re-intensification episode (Figure 11). However, the intense lightning phenomenon around 16 UT on 27 July (Figure 13) occurred almost simultaneously with the typhoon intensity peak, which was maintained for ~6 h before it rapidly decreased. Thus, the occurrence of intense lightning in the inner-core region cannot always be used as an accurate predictor of the rapid intensification of a typhoon.

4. Conclusions

Using lightning observation data from the World-Wide Lightning Location Network (WWLLN), ERA5 reanalysis data, and cloud-image data from the Himawari-8/9 satellite, intense lightning phenomena that occurred during the lifetime of Super Typhoon Doksuri (2023) were analyzed, which yielded the following main results:

1. Lightning activity in the typhoon's outer rainband exhibited an intermittent outbreak feature. The occurrence of intense lightning was mainly ascribed to deep convections, and the violent vertical motions inside the typhoon provided favorable thermodynamic conditions (i.e., a high CAPE index, abundant water vapor, and an extremely low cloud-top brightness temperature) for the formation of intense lightning through the non-inductive charging mechanism.

2. The occurrence of inner-core intense lightning was closely related to the rapid intensification of the typhoon and the adjustment of its internal structure. In the first rapid-intensification episode, intense inner-core lightning preceded the typhoon intensity peak by about 14–41 h, whereas it occurred ~9 h after the typhoon peak during the re-intensification episode. Inner-core lightning may therefore serve as a potential precursor of a typhoon's rapid intensification, but its predictive value is conditional rather than universal.

Numerical simulations of the formation of intense lightning flashes were conducted using the E-WRF model, and the observed intense lightning phenomena were interpreted based on the non-inductive charging mechanism. Deep convections inside the typhoon provided a favorable environment for intracloud microphysical electrification processes, and intense lightning was triggered when the established intracloud electric field was stronger than the breakdown thresholds. In the typhoon's landfall stage, the orographic lifting and island thermal effects may have contributed to the intense lightning outbreaks. In recent decades, due to global warming, typhoon activity and intensity have shown increasing trends in the Western Pacific [46]. Research on the regional characteristics and formation mechanisms of lightning activity in typhoons contributes to our understanding of lightning phenomena in special meteorological systems and to typhoon forecasting

over the South China Sea. In the future, typhoon-associated lightning phenomena should be further studied using experimental observations from multiple instruments and theoretical simulations from different models; the effects of orographic lifting and thermal islands should also be further investigated.

Supplementary Materials: The following supporting information can be downloaded at: https://www.mdpi.com/article/10.3390/rs18213808/s1, Python (PyCharm_2025.1.1.1) scripts used in this study are available at: https://doi.org/10.5281/zenodo.22205936, Python script 1: BTD.py; Python script 2: WRF_ELEC.py.

Author Contributions: Conceptualization, S.G. and G.L.; methodology, G.L., X.C. and S.G.; software, X.H., H.H. and S.G.; validation, S.G., G.L. and X.C.; formal analysis, S.G. and X.H.; investigation, S.G., X.H., and H.H.; resources, G.Y., F.L. and J.J.; data curation, X.C., X.H., and Z.Y.; writing—original draft preparation, S.G. and X.H.; writing—review and editing, S.G.; visualization, X.H.; supervision, S.G., G.L. and G.Y.; project administration, G.L. and G.Y.; funding acquisition, S.G. All authors have read and agreed to the published version of the manuscript.

Funding: This research was funded by the National Natural Science Foundation of China (42364012), the Innovational Fund for Scientific and Technological Personnel of Hainan Province (KJRC2023C05), and Project Supported by the Specialized Research Fund for State Key Laboratories.

Data Availability Statement: The datasets analyzed in this study are publicly available from the World Wide Lightning Location Network (WWLLN), ECMWF ERA5 reanalysis dataset, Japan Meteorological Agency Himawari-8/9 satellite observations, and China Meteorological Administration tropical cyclone best-track dataset. The E-WRF model output generated in this study is available from the corresponding author upon reasonable request. More details about the data and software associated with this manuscript are published on Zenodo at https://doi.org/10.5281/zenodo.22205936 [47].

Acknowledgments: The authors wish to thank the World Wide Lightning Location Network (http://wwlln.net, accessed on 2 September 2026), a collaboration among over 50 universities and institutions, for providing the lightning location data used in this paper. We acknowledge the Japan Meteorological Agency (JMA) for the Himawari-8/9 satellite observations, the European Centre for Medium-Range Weather Forecasts (ECMWF) for the ERA5 reanalysis data, and the China Meteorological Administration (CMA) for the tropical cyclone best-track dataset.

Conflicts of Interest: The authors declare no conflicts of interest.

References

1. Takahashi, T. Riming electrification as a charge generation mechanism in thunderstorms. *J. Atmos. Sci.* **1978**, *35*, 1536–1548.
2. Black, R.A.; Hallett, J. Observation of the distribution of ice in hurricanes. *J. Atmos. Sci.* **1986**, *43*, 802–822.
3. Abarca, S.F.; Corbosiero, K.L.; Vollaro, D. The World Wide Lightning Location Network and convective activity in tropical cyclones. *Mon. Weather Rev.* **2011**, *139*, 175–191.
4. Fierro, A.O.; Mansell, E.R.; MacGorman, D.R.; Ziegler, C.L. The implementation of an explicit charging and discharge lightning scheme within the WRF-ARW model: Benchmark simulations of a continental squall line, a tropical cyclone, and a winter storm. *Mon. Weather Rev.* **2013**, *141*, 2390–2415.
5. Price, C.; Asfur, M.; Yair, Y. Maximum hurricane intensity preceded by increase in lightning frequency. *Nat. Geosci.* **2009**, *2*, 329–332.
6. Corbosiero, K.L.; Molinari, J. The effects of vertical wind shear on the distribution of convection in tropical cyclones. *Mon. Weather Rev.* **2002**, *130*, 2110–2123.
7. Wang, F.; Qie, X.; Wang, D.; Liu, D.; Yang, P. Lightning activity in tropical cyclones and its relationship to dynamic and thermodynamic parameters over the Northwest Pacific. *Atmos. Res.* **2018**, *213*, 86–96.

8. Zhang, W.; Zhang, Y.; Shu, S.; Zheng, D.; Xu, L. Lightning distribution in tropical cyclones making landfall in China. *Front. Earth Sci.* **2022**, *10*, 940205.
9. Naccarato, K.P.; Pinto, O., Jr.; Pinto, I.R.C.A. Evidence of thermal and aerosol effects on the cloud-to-ground lightning density and polarity over large urban areas of southeastern Brazil. *Geophys. Res. Lett.* **2003**, *30*, 1674.
10. Kumar, P.R.; Kamra, A.K. Lightning activity variations over three islands in a tropical monsoon region. *Atmos. Res.* **2010**, *98*, 309–316.
11. Zhang, W.J.; Zhang, Y.; Zheng, D.; Zhou, X. Lightning distribution and eyewall outbreaks in tropical cyclones during landfall. *Mon. Weather Rev.* **2012**, *140*, 3573–3586.
12. Lu, J.; Qie, X.; Xiao, X.; Jiang, R.; Mansell, E.R.; Fierro, A.O.; Liu, D.; Chen, Z.; Yuan, S.; Sun, M.; et al. Effects of convective mergers on the evolution of microphysical and electrical activity in a severe squall line simulated by WRF coupled with explicit electrification scheme. *J. Geophys. Res. Atmos.* **2022**, *127*, e2021JD036398.
13. Kang, H.; Jayaratne, R.; Williams, E. A new model for charge separation by proton transfer during collision between ice particles in thunderstorms. *J. Geophys. Res. Atmos.* **2023**, *128*, e2023JD038626.
14. Lu, X.Q.; Yu, H.; Ying, M.; Zhao, B.; Zhang, S.; Lin, L.; Bai, L.; Wan, R. Western North Pacific tropical cyclone database created by the China Meteorological Administration. *Adv. Atmos. Sci.* **2021**, *38*, 690–699. https://doi.org/10.1007/s00376-020-0211-7.
15. Rodger, C.J.; Werner, S.; Brundell, J.B.; Lay, E.H.; Thomson, N.R.; Holzworth, R.H.; Dowden, R.L. Detection efficiency of the VLF World-Wide Lightning Location Network (WWLLN): Initial case study. *Ann. Geophys.* **2006**, *24*, 3197–3214. https://doi.org/10.5194/angeo-24-3197-2006.
16. Hutchins, M.L.; Holzworth, R.H.; Brundell, J.B.; Rodger, C.J. Far-field power of lightning strokes as measured by the World Wide Lightning Location Network. *J. Atmos. Ocean. Technol.* **2012**, *29*, 1102–1110. https://doi.org/10.1175/JTECH-D-11-00174.1.
17. Zhang, W.; Hui, W.; Lyu, W.; Cao, D.; Li, P.; Zheng, D.; Fang, X.; Zhang, Y. FY-4A LMI observed lightning activity in Super Typhoon Mangkhut (2018) in comparison with WWLLN data. *J. Meteorol. Res.* **2020**, *34*, 336–352. https://doi.org/10.1007/s13351-020-9500-4.
18. Zhu, X.; Lu, G.P.; Sun, L.; Zhuge, X.; Zhang, W.; Zhou, R.; Cheng, Z.; Cohen, M.B. Enhanced lightning activity during the merger of Super Typhoon Hinnamnor (2022) with a southern tropical depression. *Adv. Atmos. Sci.* **2026**, *43*, 1243–1255. https://doi.org/10.1007/s00376-025-4515-5.
19. Hutchins, M.L.; Holzworth, R.H.; Virts, K.S.; Wallace, J.M.; Heckman, S. Radiated VLF energy differences of land and oceanic lightning. *Geophys. Res. Lett.* **2013**, *40*, 2390–2394. https://doi.org/10.1002/grl.50406.
20. Fan, P.L.; Zheng, D.; Zhang, Y.J.; Gu, S.; Zhang, W.; Yao, W.; Yan, B.; Xu, Y. A performance evaluation of the World Wide Lightning Location Network (WWLLN) over the Tibetan Plateau. *J. Atmos. Ocean. Technol.* **2018**, *35*, 927–939. https://doi.org/10.1175/JTECH-D-17-0144.1.
21. Hersbach, H.; Bell, B.; Berrisford, P.; Hirahara, S.; Horányi, A.; Muñoz-Sabater, J.; Nicolas, J.; Peubey, C.; Radu, R.; Schepers, D.; et al. The ERA5 global reanalysis. *Q. J. R. Meteorol. Soc.* **2020**, *146*, 1999–2049. https://doi.org/10.1002/qj.3803.
22. Bessho, K.; Date, K.; Hayashi, M.; Ikeda, A.; Imai, T.; Inoue, H.; Kumagai, Y.; Miyakawa, T.; Murata, H.; Ohno, T.; et al. An introduction to Himawari-8/9—Japan's new-generation geostationary meteorological satellites. *J. Meteorol. Soc. Jpn. Ser. II* **2016**, *94*, 151–183. https://doi.org/10.2151/jmsj.2016-009.
23. Zhang, Z.; Wu, W.; Fan, M.; Tao, M.; Wei, J.; Jin, J.; Wang, Q. Validation of Himawari-8 aerosol optical depth retrievals over China. *Atmos. Environ.* **2019**, *199*, 32–44. https://doi.org/10.1016/j.atmosenv.2018.11.024.
24. Yang, Y.; Zhao, C.; Fan, H. Spatiotemporal distributions of cloud properties over China based on Himawari-8 Advanced Himawari Imager data. *Atmos. Res.* **2020**, *240*, 104927. https://doi.org/10.1016/j.atmosres.2020.104927.
25. Baum, B.A.; Menzel, W.P.; Frey, R.A.; Tobin, D.C.; Holz, R.E.; Ackerman, S.A.; Heidinger, A.K.; Yang, P. MODIS cloud-top property refinements for Collection 6. *J. Appl. Meteorol. Climatol.* **2012**, *51*, 1145–1163. https://doi.org/10.1175/JAMC-D-11-0203.1.
26. Ester, M.; Kriegel, H.-P.; Sander, J.; Xu, X. A density-based algorithm for discovering clusters in large spatial databases with noise. In Proceedings of the Second International Conference on Knowledge Discovery and Data Mining (KDD-96), Portland, OR, USA, 2–4 August 1996; pp. 226–231. https://dl.acm.org/doi/10.5555/3001460.3001507.
27. Mansell, E.R.; MacGorman, D.R.; Ziegler, C.L.; Straka, J.M. Charge structure and lightning sensitivity in a simulated multicell thunderstorm. *J. Geophys. Res. Atmos.* **2005**, *110*, D12101. https://doi.org/10.1029/2004JD005287.
28. Sakradzija, M.; Seifert, A.; Dipankar, A. A stochastic scale-aware parameterization of shallow cumulus convection across the convective gray zone. *J. Adv. Model. Earth Syst.* **2016**, *8*, 786–812. https://doi.org/10.1002/2016MS000634.
29. Bian, G.; Tang, J.; Wang, S.; Fang, J. Regional climate simulation of tropical cyclone at gray-zone resolution over Western North Pacific: With/without cumulus parameterization. *Clim. Dyn.* **2023**, *61*, 3179–3194. https://doi.org/10.1007/s00382-023-06740-8.

30. Hong, S.Y.; Noh, Y.; Dudhia, J. A new vertical diffusion package with an explicit treatment of entrainment processes. *Mon. Weather Rev.* **2006**, *134*, 2318–2341. https://doi.org/10.1175/MWR3199.1.
31. Iacono, M.J.; Delamere, J.S.; Mlawer, E.J.; Shephard, M.W.; Clough, S.A.; Collins, W.D. Radiative forcing by long-lived greenhouse gases: Calculations with the AER radiative transfer models. *J. Geophys. Res. Atmos.* **2008**, *113*, D13103. https://doi.org/10.1029/2008JD009944.
32. Dudhia, J. Numerical study of convection observed during the Winter Monsoon Experiment using a mesoscale two-dimensional model. *J. Atmos. Sci.* **1989**, *46*, 3077–3107. https://doi.org/10.1175/1520-0469(1989)046%3c3077:NSOCOD%3e2.0.CO;2.
33. Mansell, E.R.; Ziegler, C.L.; MacGorman, D.R. Simulated electrification of a small thunderstorm with two-moment bulk microphysics. *J. Atmos. Sci.* **2010**, *67*, 171–194. https://doi.org/10.1175/2009JAS2965.1.
34. Tomassini, L.; Field, P.R.; Honnert, R.; Malardel, S.; McTaggart-Cowan, R.; Saitou, K.; Noda, A.T.; Seifert, A. The "grey zone" cold air outbreak global model intercomparison: A cross evaluation using large-eddy simulations. *J. Adv. Model. Earth Syst.* **2017**, *9*, 39–64. https://doi.org/10.1002/2016MS000822.
35. Chen, F.; Dudhia, J. Coupling an advanced land surface-hydrology model with the Penn State-NCAR MM5 modeling system. Part I: Model implementation and sensitivity. *Mon. Weather Rev.* **2001**, *129*, 569–585. https://doi.org/10.1175/1520-0493(2001)129%3c0569:CAALSH%3e2.0.CO;2.
36. Jiménez, P.A.; Dudhia, J.; González-Rouco, J.F.; Navarro, J.; Montávez, J.P.; García-Bustamante, E. A revised scheme for the WRF surface layer formulation. *Mon. Weather Rev.* **2012**, *140*, 898–918. https://doi.org/10.1175/MWR-D-11-00056.1.
37. Squires, K.; Businger, S. The morphology of eyewall lightning outbreaks in two Category 5 hurricanes. *Mon. Weather Rev.* **2008**, *136*, 1706–1726. https://doi.org/10.1175/2007MWR2150.1.
38. Iudin, D.I.; Rakov, V.A.; Syssoev, A.A.; Bulatov, A.A.; Hayakawa, M. From decimeter-scale elevated ionic conductivity regions in the cloud to lightning initiation. *Sci. Rep.* **2021**, *11*, 18016. https://doi.org/10.1038/s41598-021-97321-4.
39. Peeters, S.A.; Mirpour, S.; Köhn, C.; Nijdam, S. A model for positive corona inception from charged ellipsoidal thundercloud hydrometeors. *J. Geophys. Res. Atmos.* **2022**, *127*, e2021JD035505.
40. Bolton, D. The computation of equivalent potential temperature. *Mon. Weather Rev.* **1980**, *108*, 1046–1053. https://doi.org/10.1175/1520-0493(1980)108%3c1046:TCOEPT%3e2.0.CO;2.
41. Deierling, W.; Petersen, W.A. Total lightning activity as an indicator of updraft characteristics. *J. Geophys. Res. Atmos.* **2008**, *113*, D16210. https://doi.org/10.1029/2007JD009598.
42. Chan, J.C.L.; Liu, K.S.; Ching, S.E.; Lai, E.S.T. Asymmetric distribution of convection associated with tropical cyclones making landfall along the South China Coast. *Mon. Weather Rev.* **2004**, *132*, 2410–2420. https://doi.org/10.1175/1520-0493(2004)132%3c2410:ADOCAW%3e2.0.CO;2.
43. Williams, E.; Chan, T.; Boccippio, D. Islands as miniature continents: Another look at the land-ocean lightning contrast. *J. Geophys. Res. Atmos.* **2004**, *109*, D16206. https://doi.org/10.1029/2003JD003833.
44. Rogers, R.F.; Reasor, P.D.; Lorsolo, S. Airborne Doppler observations of the inner-core structural differences between intensifying and steady-state tropical cyclones. *Mon. Weather Rev.* **2013**, *141*, 2970–2991. https://doi.org/10.1175/MWR-D-12-00357.1.
45. Fierro, A.O.; Simpson, J.A.; LeMone, M.A.; Straka, J.M.; Smoot, R. Evolution of eyewall convective events as indicated by intracloud and cloud-to-ground lightning activity during the rapid intensification of hurricanes Rita and Katrina. *Mon. Weather Rev.* **2011**, *139*, 1492–1508. https://doi.org/10.1175/2010MWR3532.1.
46. Li, X.; Zhan, R.; Wang, Y.; Zhao, J.; Ding, Y.; Song, K. Recent increase in rapid intensification events of tropical cyclones along China Coast. *Clim. Dyn.* **2024**, *62*, 331–344. https://doi.org/10.1007/s00382-023-06917-1.
47. He, X. Data Statement for Article "Insights into Intensive Lightning Activity in the Lifetime of Super Typhoon Doksuri (2023)" [Data Set]. *Zenodo* 2026. Available online: https://zenodo.org/records/22205936 (accessed on 2 September 2026).

Disclaimer/Publisher's Note: The statements, opinions and data contained in all publications are solely those of the individual author(s) and contributor(s) and not of MDPI and/or the editor(s). MDPI and/or the editor(s) disclaim responsibility for any injury to people or property resulting from any ideas, methods, instructions or products referred to in the content.